Geological Society of America
Special Paper 356
2002

# *Modeling long-term climatic effects of impacts: First results*

**Thomas Luder**
**Willy Benz**
**Thomas F. Stocker**
*Physics Institute, University of Bern, Sidlerstrasse 5, CH-3012 Bern, Switzerland*

## ABSTRACT

**Catastrophic impacts of asteroids or comets on Earth are events that have occurred in the past and will happen in the future. While climate perturbations induced by an impact-generated dust cloud have been studied in recent years, the studies have been restricted to the first year following the event. The aim of this study is to assess the long-term response of the climate including ocean circulation following the impact of a 5-km-diameter asteroid.**

**We modeled the dust evolution, calculated radiation transfer through dust layers, and used a zonally averaged, coupled ocean-atmosphere model to obtain the climatic response. Within less than one year, mean sea surface temperatures (SST) dropped by ~2 °C. Even though most of the dust had been removed from the atmosphere after several months, SST deviations remained larger than 0.1 °C for a period of 20 yr following impact. In the first year, ocean temperatures below 500 m depth did not change. Although 60 yr later the main temperature deviations were still located above 1000 m depth, temperature changes occurred throughout the ocean. After 2000 yr the oceans showed slightly increased temperatures. A zone below the surface of the northern Atlantic exhibited increased temperatures by 3 °C. Precipitations decreased within months to about half of normal, but recovered after 1 yr. We did not observe glaciation effects.**

## INTRODUCTION

Temperature drops and darkness lasting for months are some of the outcomes triggered by impacts of asteroids and comets on the Earth. The wide range of effects (see review by Toon et al., 1997) starts with an air blast and seismic waves; the destruction scale depends on the impactor size, but ranges from local for 1 km bolides to continental for 10 km objects. Ocean impacts induce tsunamis, which threaten coastal regions (Hills et al., 1994; Ward and Asphaug, 2000). It is also presumed that part of the global land biomass catches fire (Wolbach et al., 1990) due to the impact ejecta energy deposition into the atmosphere (Melosh et al., 1990). Chemical effects such as the release of nitric oxide (Zahnle, 1990), worldwide acid rain (Lewis et al., 1982; Prinn and Fegley, 1987), and destruction of the ozone layer have also been invoked.

The globally distributed ejecta in the stratosphere perturbs the radiation budget of air, land, and water on Earth. Larger fragments settle rapidly, whereas submicrometer dust particles remain in the stratosphere for months (Toon et al., 1982). If the impact releases sulfur (Pope et al., 1994, 1997; Kring et al., 1996; Pierazzo et al., 1998), sulfuric acid aerosols could be found in the atmosphere for years. Because of their long residence times in the air and their interaction with radiation, small dust particles and, if released, sulfuric acid aerosols disturb the climate. The effect of impact-induced dust on global tempera-

Luder, T., Benz, W., and Stocker, T.F., 2002, Modeling long-term climatic effects of impacts: First results, *in* Koeberl, C., and MacLeod, K.G., eds., Catastrophic Events and Mass Extinctions: Impacts and Beyond: Boulder, Colorado, Geological Society of America Special Paper 356, p. 717–729.

tures has been investigated with one-dimensional radiative-convective atmospheric models (Toon et al., 1982) and with three-dimensional atmospheric general circulation models (Covey et al., 1990, 1994). The focus has been on changes in the atmosphere, whereby the underlying surface has been taken into account as a heat reservoir. Typically a zero heat capacity was chosen for continental areas. Oceans were represented with either infinite or finite heat capacities. While in the former case these simulations are appropriate only as long as the sea temperatures have not reacted to the perturbation, in the latter case the sea is approximated by static oceans, and influences and changes in the circulation are neglected. Therefore, the time span integrated by these models is usually restricted to 1 yr.

To consider climatic changes on time scales of centuries to millennia, we use a low-order coupled ocean-atmosphere model for paleoclimate studies, coupled to a multiscattering radiative transfer and a dust evolution simulation code. We discuss assumptions and present our model, and then report on climatic results.

The results do not necessarily reflect the Cretaceous-Tertiary (K-T) event, because this study investigates climatic effects of an impact with the present oceanic configuration and the present climate, and because the amount of dust considered corresponds to a smaller impactor (5 km) than the K-T bolide. We regard this work as a contribution to the exploration of the consequences of a collision with an asteroid or comet today. However, we think that similar effects might have occurred after real impacts in the past.

## ASSUMPTIONS AND MODEL

### *Organization of the model*

Model simulations of the K-T ejecta trajectories give evidence of a nonspherical symmetric distribution of the dust around the globe (Argyle, 1988; Durda et al., 1997). However, for simplicity, we assume in this study that the dust has spread out globally and that the distribution does not depend on geographical location. Thus horizontal motions of dust are not allowed in the model. The temporal development of the dust layer in the stratosphere is modeled with a one-dimensional dust evolution code that takes into account the settling and the coagulation processes of dust particles. A multiscattering radiation transfer code calculates solar and infrared energy fluxes through the dust layer specified by the dust evolution model. The energy fluxes depend on a set of parameters, including the solar position and the temperature of the underlying ocean. An ocean circulation model simulates the response of the climate to the perturbed energy fluxes.

### *Initial dust distribution after the impact*

The plume of melted and vaporized target and impactor expands at velocities of the order of Earth's escape velocity and pervades the atmosphere. Once these particles have left the vicinity of the atmosphere, their orbits become pure Keplerian. Some of this material will leave the Earth, and some moves at altitudes of hundreds of kilometer around the globe. Then it reenters the atmosphere from above. This takes place at all locations around the Earth only hours after the ejection (Melosh et al., 1990). Thus, compared to the lifetime of dust particles in the atmosphere, the dust is assumed to be distributed both instantaneously and globally. Therefore, our model starts with the dust already spread worldwide and uniformly.

A good guess of the size of ejected particles is taken from the size distribution of volcanic dust (Toon et al., 1982). Farlow et al. (1981) measured sizes of aerosols collected in the stratosphere between and after the eruptions of Mount St. Helens, and fitted the results with log-normal size distributions. They found mode radii $r_0$ from 0.48 $\mu$m to 0.94 $\mu$m. For aerosols in the stratosphere 1 yr after an average volcanic eruption, Jaenike (1988) gave a log-normal size distribution with a mode radius of $\sim$0.217 $\mu$m. This value is smaller than the radii from Farlow et al. (1981) because the size distribution by Farlow et al. (1981) refers to samples of fresh volcanic aerosols, while the data given by Jaenike (1988) represent an evolved population. In 1 yr the larger particles have moved out of the stratosphere faster than smaller particles; therefore, the size distribution shifts to the smaller sizes.

In their investigation of the evolution of an impact-induced dust cloud, Toon et al. (1982) used a log-normal particle size distribution with $r_0 = 0.5$ $\mu$m. They stated a low sensitivity of the cloud evolution to changes in the mode radius $r_0$. In our model the amount of dust in the stratosphere after the impact is insensitive to the value of $r_0$ in the interval between 0.5 $\mu$m and 0.9 $\mu$m. We conclude that the precise value is not critical. We use a log-normal size distribution with mode radius $r_0$ of 0.7 $\mu$m, which is in the range of the values given by Farlow et al. (1981) for the fresh volcanic aerosols.

At the larger end of the size distribution we neglect all particles with diameter larger than 4 $\mu$m for several reasons. (1) Farlow et al. (1981) found no particles larger than 3 $\mu$m in diameter. (2) Because the fall speed of large particles is high, they are quickly removed from the atmosphere by settling and washout before they have an influence on the climate (Toon et al., 1997). (3) Because of the steepness of the size distribution, their number is smaller by several orders of magnitude than the particles with the typical radius of 0.7 $\mu$m. To appraise the total initial amount of dust, we use the estimate by Toon et al. (1997) that the mass of submicrometer dust reaching the stratosphere equals a fraction $\alpha = 30\%$ of the impactor's mass, which is a small fraction of the total ejecta. Let $R$, $d$, and $\rho$ denote the radius of the Earth, the impactor diameter, and its density, respectively. Then the mass of the impactor and the surface area of the Earth are $\pi \cdot \rho \cdot d^3/6$ and $4 \cdot \pi \cdot R^2$. Hence, if the dust is distributed worldwide, the column density of dust is given by

$$L = \alpha \cdot \rho \cdot d^3/(24 \cdot R^2) \qquad (1)$$

(Fig. 1). In the climate simulation of this study we use a dust load of $L = 100$ g/m$^2$, which corresponds to a bolide with diameter of ~5 km and a density of 3000 kg/m$^3$.

For simplicity we assume that the number density of the particles does not depend on height at the beginning. Therefore, our model distributes the dust homogeneously along the vertical axis. Toon et al. (1982) injected the initial dust in two scenarios, between 12 km and 42 km, and between 66 km and 88 km. They found that the optical depth of an evolving dust layer is only slightly sensitive to the initial height of the particles. Covey et al. (1990) inserted the dust at altitudes from ~15 to 30 km. We set the initial lower and upper boundaries of the dust layer at $z = 20$ km and $z = 100$ km, respectively. Variations in the upper boundary do not change the evolution of the dust layer, because the Stoke's settling velocities of dust particles at these high levels are of ~100 m/s. To move from 100 km height to 80 km or 60 km takes <1 h or ~1 d, respectively, for all particles. Because total dust evolution and climatic change occur on time scales of weeks to months and even years, these initial differences in dust layer are not important. However, fall velocities of micrometer particles in the lower stratosphere are ~1 mm/s. Thus, it is not probable that impact-formed particles can be found at the lower boundary of the stratosphere around the globe shortly after they have penetrated the atmosphere from above. Therefore, we do not set the lower initial dust boundary at the tropopause but higher, at 20 km.

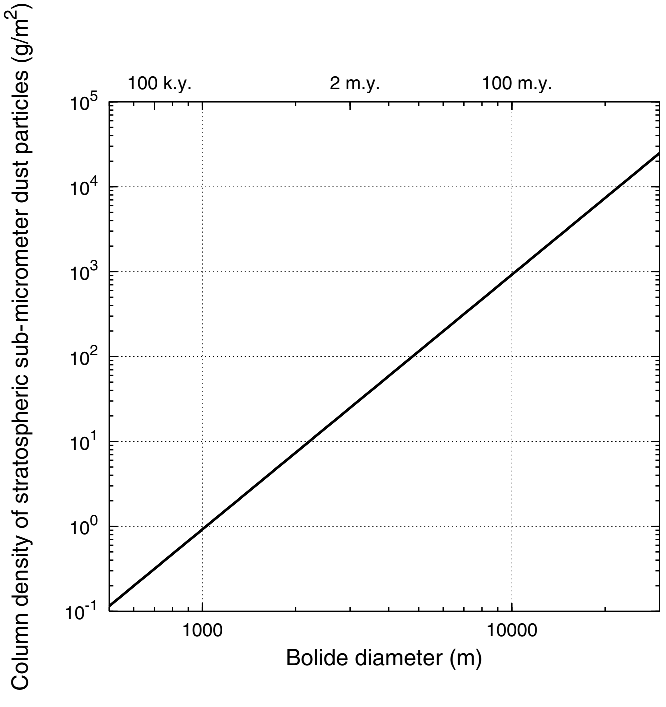

Figure 1. Amount of globally distributed submicrometer dust particles lofted by impacts into stratosphere from equation 1 (see text), assuming impactor density of 3000 kg/m$^3$. Column density of 1 g/m$^2$ corresponds to global dust mass of $5.1 \times 10^{14}$ g. For comparison, density of sheet of paper is ~50–100 g/m$^2$. Upper abscissa indicates time intervals between impacts of bodies of given size or larger (from Fig. 1 in Morrison et al., 1994).

In our simulations, dust grains are assumed spherical, which is a crude simplification of their natural shapes. However, this assumption greatly simplifies the calculation of scattering and absorption cross sections of electromagnetic waves.

### *Dust evolution model*

The dust is specified by the particle size distribution as a function of time and height in the atmosphere. The distribution evolves with time due to coagulation and sedimentation processes, which are the main mechanisms that alter the local number of particles (Toon et al., 1997).

We assume that all particles fall with a velocity that is given by the equilibrium of gravity and drag. The Stoke's drag with Cunningham slip correction factor (Otto et al., 1999) is determined by particle size, assuming spherical shape, and local parameters of the atmosphere. Thus the fall velocities depend on, among other factors, particle diameter, air temperature, and density. Large particles have a larger volume to cross-section ratio than small particles; therefore their settling speed is larger. Because the drag force increases with number density of the air molecules, and air density decreases exponentially with height, the fall speed is much smaller in lower parts of the atmosphere than in the upper parts. Thus all particles fall fast as they enter the atmosphere from above, and they slow down as they reach denser, lower atmospheric levels.

Particles collide due to different settling speeds and due to individual Brownian motion. If a collision occurs, there is a chance that the particles stick to each other. The probability is large for small relative velocities and vice versa. In the model, we use a sticking probability of unity, if the relative speed is smaller than a specific critical sticking velocity. Otherwise the particles do not stick. The critical velocity depends on the particles' radii, masses, and material constants. Analytical expressions for the sticking velocity are from Dominik and Tielens (1997), Chokshi et al. (1993), and Wurm and Blum (1998). Destruction of particles due to high-speed collisions and the influence of liquid aerosols on the coagulation of dust particles are not allowed for in the model.

The effect of coagulation is a reduction in the number of small particles and an increasing number of large ones. Because large particles settle faster than small ones, coagulation reduces the residence time of a dust layer in the atmosphere significantly. Figure 2 shows the evolution of the amount of dust in the stratosphere for five initial values of the column dust density. To simulate the sedimentation and the coagulation of the dust, we do not follow single particles but propagate the particle size distribution along the vertical axis. In the model, the atmosphere from 0 to 100 km height is divided into 1000 cells.

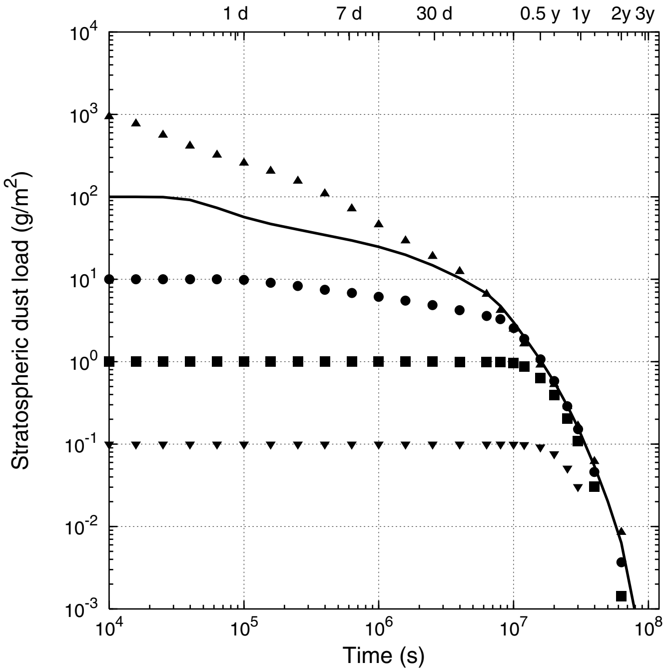

Figure 2. Total column density (load) of dust above 12 km as function of time for five initial dust loads. Solid line represents nominal case used in climate simulation. Initial loads of 1, 10, 100, or 1000 g/m$^2$ correspond to bolide diameters of ~1, 2, 5, or 10 km, respectively (Fig. 1). Due to coagulation, dust loads converge.

The dust population in every cell is represented by 100 particle volume bins.

Because the particles of all sizes drop down according to their local fall velocities, the numbers of particles in every bin obey advection equations, which are solved with an upwind difference scheme. Because all bins in every cell exchange particles due to coagulation, all advection equations are coupled. The length of the time step is determined by the stipulation that every particle of every size bin has to fulfill the equivalent of a local Courant criterion.

### *Radiation transfer calculations through the dust layer*

As far as radiation transfer is concerned, a dust layer in the atmosphere can be compared with water clouds. In contrast to soot particles, dust grains and water droplets are reflective. Consequently, parts of an electromagnetic wave impinging on a dust grain are not only absorbed but also scattered in all directions. In general, scattering dominates over absorption for visible radiation (Ramaswamy and Kiehl, 1985). Thus substantial fractions of the energy of an incident solar ray are reflected many times from particle to particle in the dust layer. Therefore, the radiation field of visible light consists of the direct, damped solar beam as well as diffuse light. Because the absorption probability for an electromagnetic wave by a dust particle is small but not zero, the wave is absorbed before it has been scattered infinite times and so not only the direct solar beam but also the diffuse light are damped. However, the penetration depth of the diffuse radiation into the layer is larger than of the direct beam. Consequently, on an overcast day, while the Sun is not visible, the environment is well illuminated due to the diffuse light from the cloud cover.

***Model.*** A single scattering model is a simplification of the radiation transfer through dust. Whereas Toon et al. (1982) used a multiscattering method to calculate the implications of a dust layer on radiation fluxes, we believe that Covey et al. (1994) neglected multiscattering effects.

In our multiscattering code, we first calculate the scattering phase function, extinction, absorption, and scattering cross sections of single spherical particles using Mie theory (Hansen and Travis, 1974; Liou, 1980; Goody and Yung, 1989). Complex indices of refraction depending on wavelength for dust-like aerosols are from Jaenike (1988). Second, we allow for the multiple scattering effects with the Doubling and Adding method (Goody and Yung, 1989). This technique starts with an optically thin sublayer of the dust cloud. In that layer, multiple scattering effects are improbable due to its tenuity. Therefore the transmission, absorption, and scattering of the thin layer can be calculated based on the radiative properties of single dust particles. Then, the Doubling and Adding method piles up two such thin layers and determines the transmission, absorption, and scattering of the resulting doubled layer. Multiple scattering between the sublayers is now taken into account explicitly. By repeating this process with the doubled layer as input, we obtain a layer with a four-fold thickness. Further repetitions of the doubling step lead quickly to layers with a large optical depth.

The energy absorbed by the dust particles has to be reemitted as infrared radiation. As a part of the total radiation field, it contributes to the net energy flux, and therefore infrared radiation has to be taken into account. We determine the temperature profile in the dust layer assuming that dust particles are in energetic equilibrium with the local radiation. The wavelengths considered range from 0.15 to 81.37 $\mu$m, divided into 63 finite bands. The wavelength range is chosen such that all typical spectra are covered: 99.99%, 99.67%, and 98.66% of the energies in the spectra of black bodies with temperatures of 6000 K, 300 K, and 200 K, respectively, are within this range. The results of radiation calculations depend on the number of bands, if it is below 40. However, more than 60 bands provide enough resolution on the wavelength axis.

For the radiative transfer calculations, we take the distribution of the dust from the dust evolution code. The lifetime of aerosols in the troposphere is much smaller than in the stratosphere because of rainout; therefore, we neglect all dust particles that have left the stratosphere and entered the troposphere. As concerns radiation, we assume that all absorbing gaseous constituents of the atmosphere are situated below the dust particles in the stratosphere. This splitting approach is justified by the fact that <20% of the mass of the real atmosphere is located above the tropopause. Thus in our model the radiation leaving the dust layer at its lower end does not impinge directly on the ocean surface, but is transferred through the gaseous part of the atmosphere. Due to the dust, the spectra of this light is shifted from solar toward the infrared frequencies; therefore we have to compute spectral air transmission coefficients, which depend on wavelength. These calculations are performed with MODTRAN, a "Moderate Resolution Transmittance" code, which is able to calculate atmospheric transmittance and radiance for frequencies from 0 to $1.5 \times 10^{15}$ Hz at a resolution of $6 \times 10^{10}$ Hz (Kneizys et al., 1988; Berk et al., 1989).

The radiation field in the stratospheric dust layer is determined by the boundary conditions. At the upper end we assume that the Sun is the only source of energy, and that all upward energy fluxes leave the system and are lost to space. With this, we only have to specify the position of the Sun with respect to zenith. At the lower end of the dust layer we do not allow for heat conduction between the dust layer and the underlying troposphere. Therefore, the boundary conditions at the lower end involve solar and infrared fluxes, which are given by the reflectivity and the radiative emissions of the atmospheric and oceanic cells below. These parameters are computed and specified by the model of the ocean circulation (see following).

***Results of radiation transfer calculations.*** As an example we present calculated radiative energy fluxes between a planar gray body with temperature and emissivity of 295 K and 0.95, respectively, and an overlying dust layer. The Sun is located above the layer at 36° and 64° below zenith in Figure 3 (A and B, respectively). Figure 3C represents nighttime. The radiation fluxes shown are the body's loss of energy due to its infrared emission, the gain due to the absorption of solar energy and infrared radiation from the dust, and the net flux. As expected, the solar energy absorbed decreases with the amount of dust. While column densities below 0.1 g/m$^2$ do not lead to a significant change in the amount of solar radiation, dust loads above 10 g/m$^2$ reduce the solar light by more than a factor of 10 (Fig. 3, A and B). The infrared radiation fluxes at the surface of the body are of the same magnitude as the solar flux (Fig. 3, A, B, and C). The infrared energy absorbed by the body increases with the number of dust particles having a high temperature and being optically close to the body. (Low-temperature particles and particles optically far from the body contribute only to a small extent to the infrared radiation at the lower boundary of the dust layer.) Therefore, the infrared energy increases with the thickness of the dust layer, until the optical depth of the cloud is so large that the particles at the upper boundary of the layer cannot contribute anymore to the infrared field at the lower boundary, and the infrared energy does not increase further with dust load. In the limit of dust layers with large optical depth (dust load larger than ~300 g/m$^2$), the particles at the lower boundary are decoupled from the upper boundary, in particular from the solar radiation. At the surface of the body a radiative equilibrium attunes such that the infrared emission of the dust equals the emission and the absorption of the body.

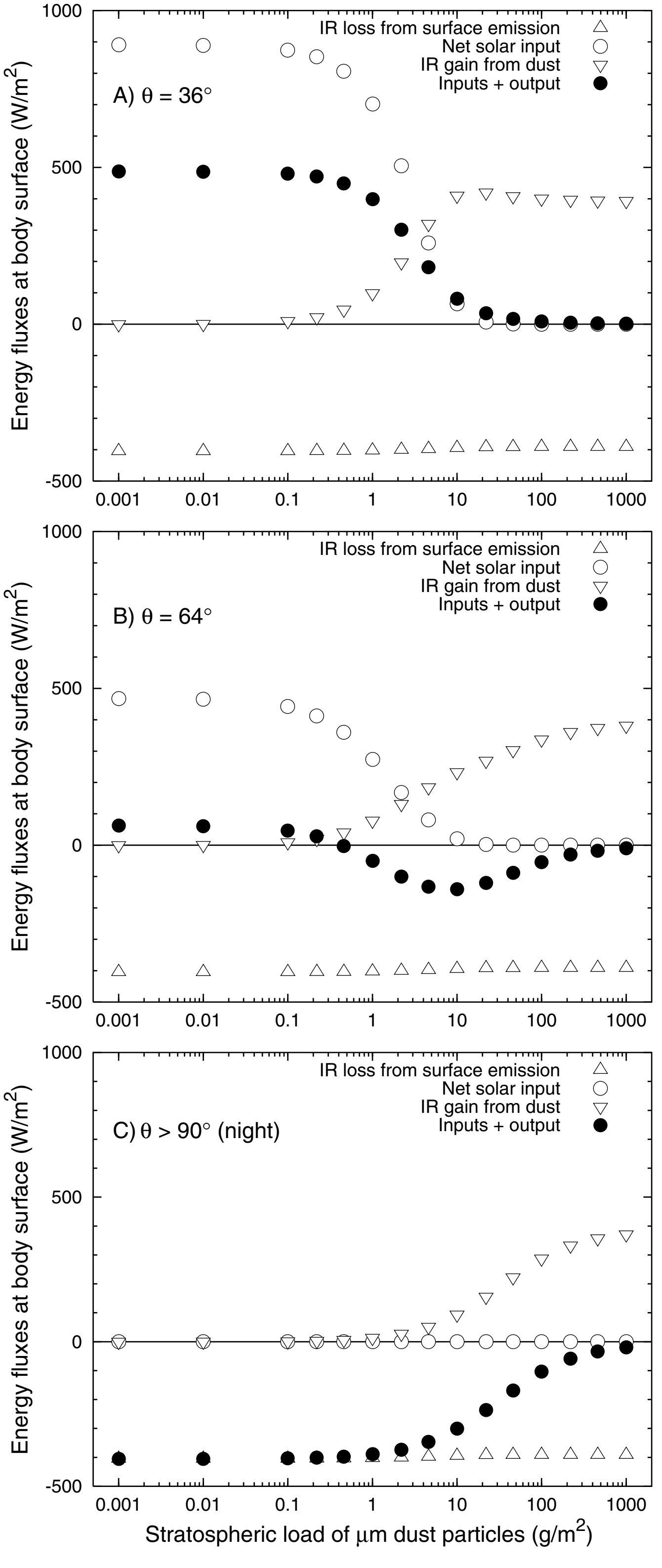

Figure 3. Examples of energy flux calculations with radiation transfer model between surface of gray body and dust layer as function of dust load. Positive energy fluxes represent energy input for body, negative values express energy output. Sun is situated above dust layer at $\theta =$ 36° and $\theta =$ 64° below zenith in A and B. C shows nighttime situation. Temperature, albedo for visible light, and infrared (IR) emissivity of body are 295 K, 0.2, and 0.95, respectively. Note minimum of total net flux at 10 g/m$^2$ dust load in B and insulation effect due to infrared emission of dust. See text for possible consequences for climate change.

Therefore, the body is radiatively insulated against space. Its radiative energy balance becomes zero.

The magnitude of this insulation due to the dust is visible in the nighttime example of Figure 3C. The emission of the body is ~400 W/m$^2$. If no dust layer covers the body, this energy is radiated to space. However, a dust load of ~1000 g/m$^2$ absorbs this flux and radiates it back to the body. Consequently we expect that diurnal terrestrial temperature variations are reduced during the presence of an impact-induced cloud.

Furthermore, the insulation leads to temperature increases in the polar regions, where the infrared emission is larger than the solar input. Therefore, with a dust layer, the reduction in solar radiation is smaller than the flux of infrared energy, which is not emitted to space but reabsorbed by the polar surface.

The combination of reduction of solar input and insulation due to dust causes an interesting effect. In the example of Figure 3B, the net energy balance of the body is not a monotonous function of amount of dust. The surface of the body undergoes a maximal energy loss of ~150 W/m$^2$ at an intermediate dust load of 10 g/m$^2$. For smaller and larger amounts of dust, the solar and the dust infrared input increase the net energy input of the body. The reason for this phenomenon is the low position of the sun, implying a smaller penetration depth than in the high solar inclination case. Therefore, at 10 g/m$^2$ dust load the solar energy at the surface is already strongly reduced. Furthermore, the dust particles heated by the Sun appear only in upper parts of the layer. More infrared radiation is emitted directly to space, and less energy reaches the surface. For dust loads larger than 10 g/m$^2$, the energy loss of the surface is smaller, because the magnitude of the insulation effect increases.

The consequence of a maximal energy loss effect at 10 g/m$^2$ might be that very large asteroid impacts lead to smaller climatic perturbations than medium-sized bolides, which produce a dust load of ~10 g/m$^2$. From equation 1 or Figure 1 we deduce that an asteroid of 1–3 km in diameter is in that range. This presumption will be investigated in a later study.

### *Thermohaline ocean circulation model*

The climatic relevance of the ocean circulation originates in the heat capacity of seawater, which is enormous compared to air. To provide an order of magnitude, we assume that the temperature in the oceans is uniform. Then it would take the Sun ~1 yr to increase the temperature of the water from 0 to 1 K. Because the ocean flows circulate cold and warm waters, they are conveyors of large vertical and horizontal energy fluxes. The heat content of the air is much smaller: a layer of ~3 m of ocean water corresponds to the total heat capacity of the atmosphere.

If less energy reaches the ocean surface as a result of an impact, the temperatures of the sea surface layer and the atmosphere decrease. However, because circulation exchanges waters between the upper layer of the ocean and underlying parts by advection, the atmosphere is, over time, brought into thermal and radiative contact with large masses of water. Therefore, the variations of air and surface water temperatures are smaller than in the case of a resting ocean. Consequently the atmospheric and climatic response depends on the circulation of the oceans.

If the investigations of the climatic changes induced by an impact are to be extended to time scales of hundreds of years, the ocean circulation has to be taken into account, not only because of its implications at the surface. The perturbations may induce a change in the ocean circulation patterns and thereby change global energy fluxes, leading to climatic effects that last longer than the residence time of the dust in the atmosphere. A hypothetical example is a decrease of the Gulf Stream, which would cause a temperature drop in Europe.

***Model.*** To investigate the long-term climatic effects, we use a two-dimensional, zonally averaged dynamic ocean circulation model (Wright and Stocker, 1992; Stocker et al., 1992). It represents the Atlantic, Indian, and Pacific basins in their present-day shape, connected with the Southern Ocean. A simple thermodynamic sea-ice model is included.

The oceanic spatial grid consists of 14 vertical and 9–14 horizontal cells, depending on the basin, with a meridional width of between 7.5° and 15°. In this model, the governing equations are written in spherical coordinates and include hydrostatic, Boussinesq, and rigid-lid approximations. Momentum equations are balances between Coriolis forces, horizontal pressure gradients, and zonal wind stress. Time-dependence enters via the equations for temperature and salinity, including vertical and meridional advection, diffusion, and convection. Horizontal and vertical eddy diffusivities are taken as constant (1000 m$^2$/s and $4 \times 10^{-5}$ m$^2$/s, respectively).

With present-day conditions this model shows the vertical current in the northern Atlantic and in the Southern Oceans, and upwelling of waters toward the surface in the Pacific and the Indian Oceans. Observed temperature and salinity patterns as well as meridional fluxes of heat and freshwater are well reproduced.

The atmospheric part does not contain a circulation model. Fluxes of energy and water within the atmosphere, between ocean and air, and between continents and oceans are parameterized in terms of surface air temperature. The model does not take into account climatic processes on land such as snow. Before the dust injection, the model oceans are in a steady state that represents the present climatic situation. At time $t = 0$ the given dust load is injected. Thereafter, the simulation progresses as the dust cloud evolves. After the column density of dust has fallen below the 0.001 g/m$^2$ level, the climate model runs for additional 2000 yr.

### *Restrictions*

Our model does not render all of the complex mechanisms that may influence the climate after an impact. We do not take into account smoke and soot particles, which are incorporated into the atmosphere by fires ignited in the aftermath of an impact. If this hypothesis is correct, then these aerosols are produced preferentially over the continents and incorporated into the atmosphere from the ground. Hence, an investigation of the climatic effects of soot and smoke has to consider the global transport of such particles in the air with three-dimensional convective models of the atmosphere, which is not in the scope of this work.

On the one hand, the radiative effects of soot particles would be a further reduction of the atmospheric transmissivity and thus a potential decrease in energy flux at the Earth's surface. On the other hand, the atmospheric albedo would be decreased due to the low reflectivity of soot. Therefore soot enhances the conversion of solar light into infrared energy. This effect could increase temperatures. We ignore variations in the densities of some air constituents, such as $H_2O$, $CO_2$, $CH_4$, $N_2O$, $SO_2$, $SO_3$, and $O_3$. In part, the amounts of change in these gases depend on the compositions of the projectile and the ground at the impact site. Therefore, studies about the climatic relevance of these atmospheric changes may refer to a specific impact. The results of the work by Pope et al. (1997) about the K-T event at Chicxulub can be applied probably only with caution to a generic impact location.

## RESULTS

We run the climate code with a scenario of an initial load of 100 g/m$^2$. The global mass of dust is $5 \times 10^{13}$ kg, which corresponds to an impactor ~5 km in diameter and 3000 kg/m$^3$ in density (Fig. 1). We discuss temperature deviations, the response of the Atlantic thermohaline circulation, and change in precipitation.

### *Global average of ocean temperatures*

The mean ocean temperature shows the global long-term behavior of the climate model (Fig. 4). The mean ocean temperature drops by 0.05 °C in the first year after the impact. It recovers to the preimpact value ~65 yr later. It increases further until 130 yr after impact. A decrease in the next 40 yr is followed by a long-term increase: 2000 yr after impact, the mean ocean temperature is 0.05 °C higher than before the impact.

The mean temperature provides a broad overview of how the modeled climate system reacts to the dust coverage. In the months with a dust-loaded atmosphere the changed radiation fluxes immediately displace the climate from its previous steady state. One year after the impact, when most of the dust particles have settled, and the energetic boundary conditions are almost equal to the conditions before the impact, the climate is not in equilibrium. During several hundreds of years the system then passes through transient states, until it comes to an equilibrium ~2000 yr after the impact. This new steady state differs from the one before the impact, pointing to a hysteresis effect.

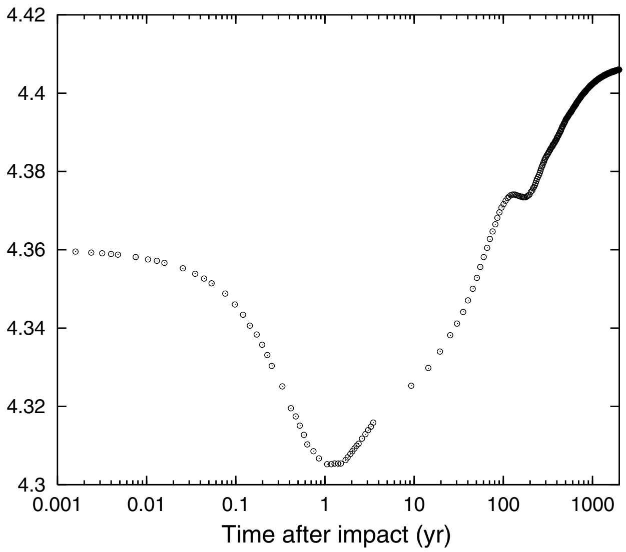

Figure 4. Mean global ocean temperature. Increase after 2000 yr is mainly due to higher temperature zone in northern Atlantic.

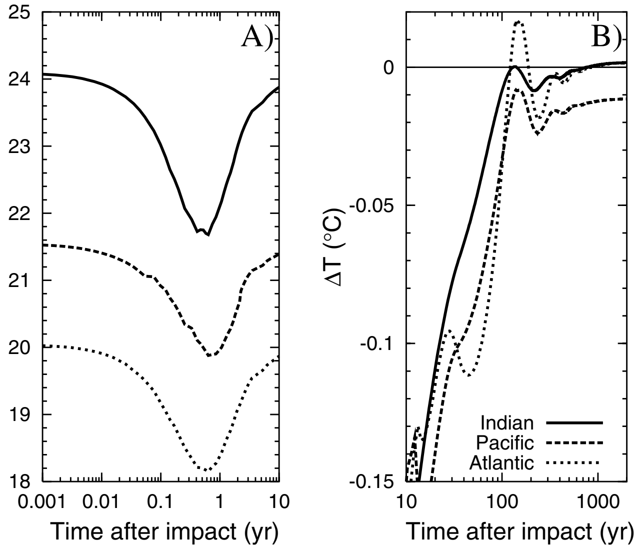

Figure 5. Mean sea surface temperatures (SSTs) for Indian, Pacific, and Atlantic Oceans in first 10 yr after impact. Maximal excursions are ~ −2.4, −1.7, and −1.9 °C, and occur between 7 and 8 months after impact. B: Deviations of SSTs with respect to values before impact from 10 to 2000 yr after impact. They are smaller than 0.1 °C for first time after 20–40 yr.

The relevance of the mean ocean temperature for biological individuals is low because different parts of an ocean respond with different amplitudes to the perturbation. Therefore, we present temperatures with spatial resolution in the following sections.

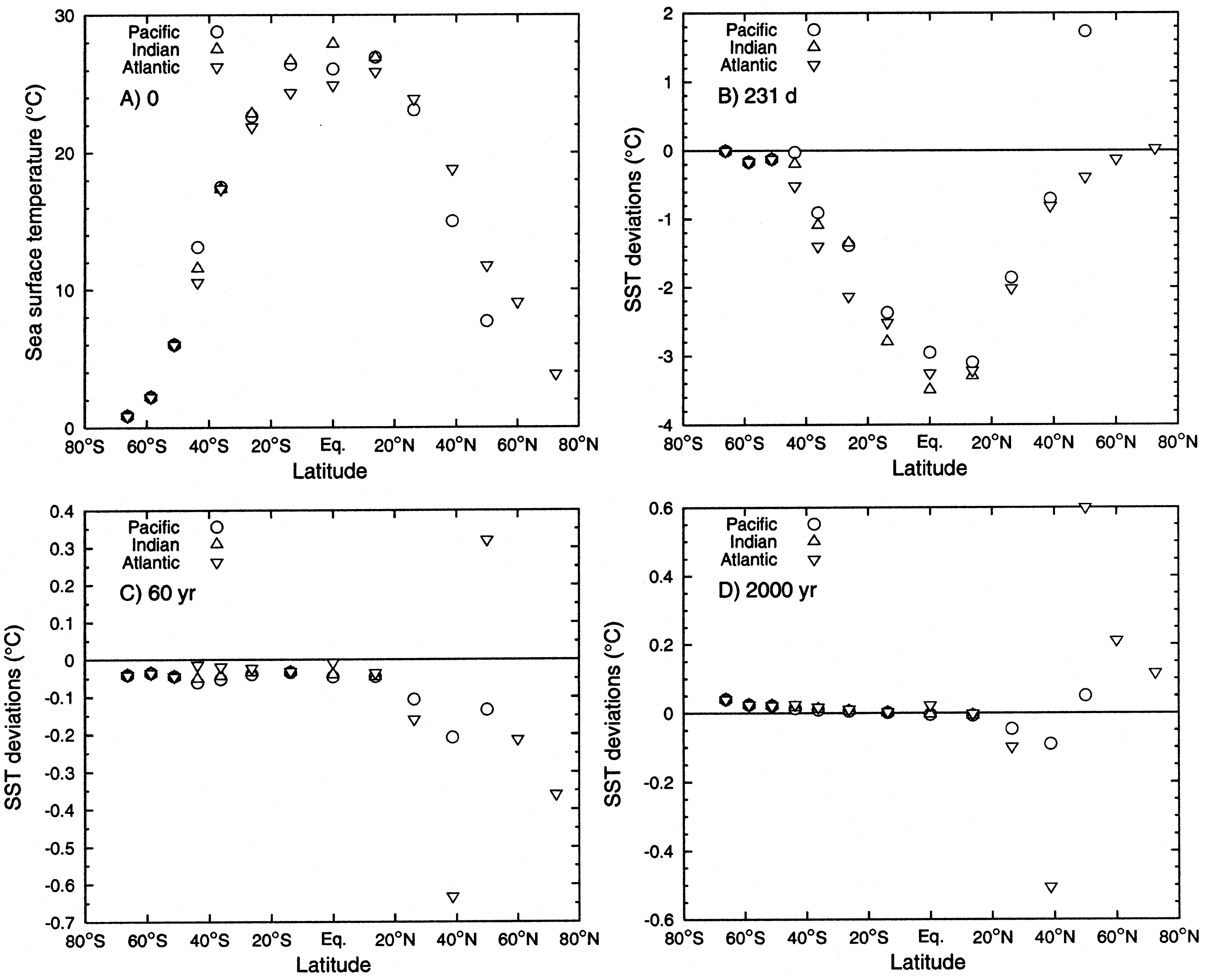

Figure 6. A: Sea surface temperatures (SSTs) in Pacific, Indian, and Atlantic Oceans before impact as function of latitude. B: Deviations of SST 231 d after impact with respect to preimpact values. C: Deviations 60 yr after impact. D: Deviations 2000 yr after impact. Identical values of all three basins in three southernmost cells come from strong coupling of oceans due to southern circumpolar current. Interpretation of deviations in northern Atlantic is given in text.

### *Sea surface temperatures*

The mean sea surface temperatures (SSTs) of the Indian, Pacific, and Atlantic Oceans drop sharply following the impact (Fig. 5A). Peak amplitudes of $\sim -2$ °C are reached after 7–8 months, after which time the temperatures recover. However, 2 yr after the impact, the deviations are still more than $-0.1$ °C (Fig. 5B), followed by small variations on a time scale of 200 yr.

Figure 6 (A–D) shows SSTs in the Indian, Pacific, and Atlantic as a function of latitude before and after the impact. Figure 6B reflects the SST 7–8 months after impact, when the deviations are maximal. By that time, the dust has been diluted by a factor of more than 100, reaching a load of 1 g/m$^2$ in absolute terms (Fig. 2). The largest coolings of more than 3 °C appear at the equator. Because the radiative energy losses are much smaller near the poles than at the equator, the drops of SST at high latitude are not as large as at low latitudes at this early time. In the northern Pacific the surface temperatures have increased by 1.7 °C. However, the waters in the northern Atlantic will show a further decrease in temperature, because the thermohaline circulation transports less energy than before from the cooled equatorial regions into the polar zone.

After 3 yr the dust column density has fallen to such low levels that the radiation transfer has recovered its initial value. Nevertheless, as is shown by the evolution of the mean sea

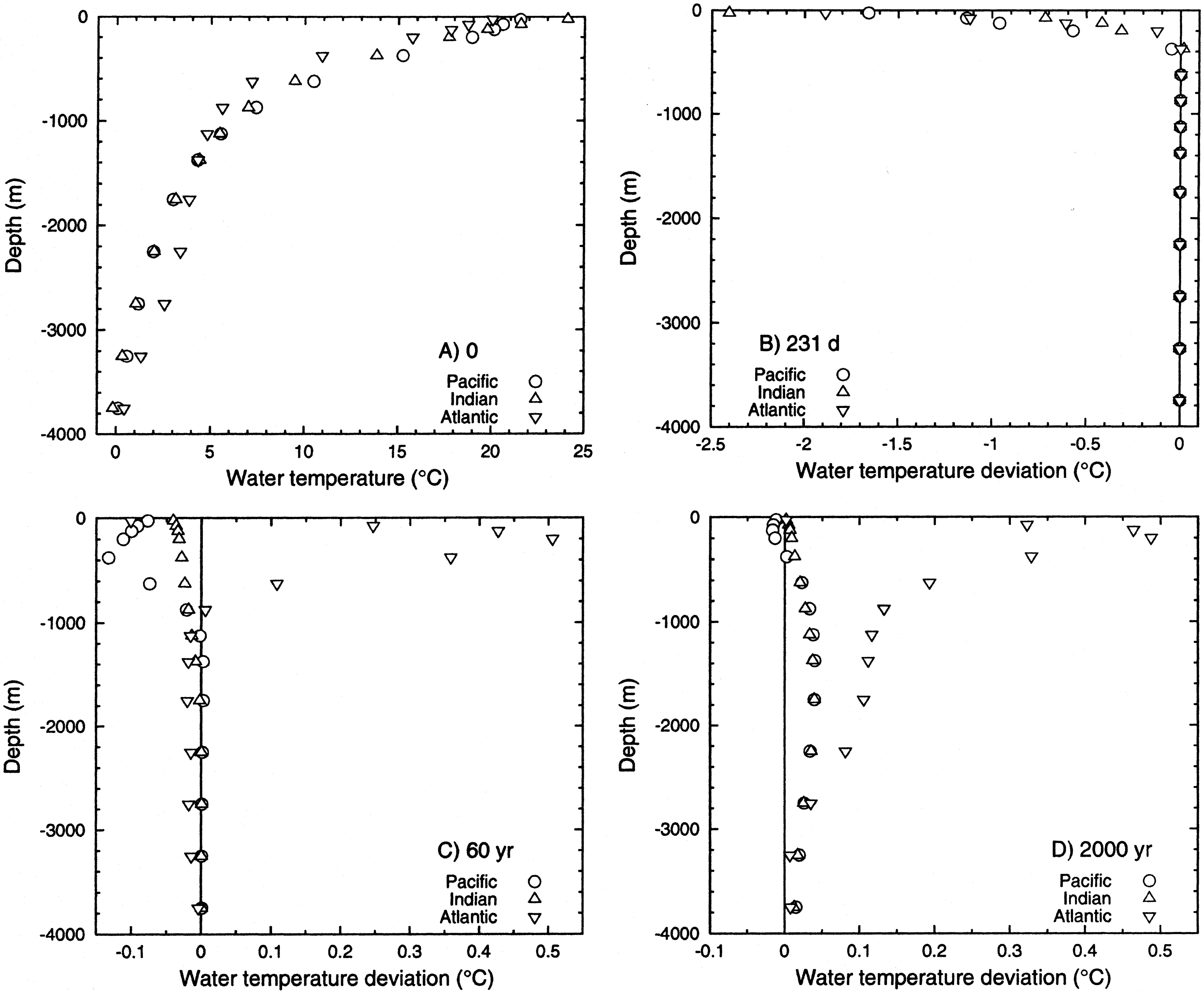

Figure 7. A: Water temperature profiles in Pacific, Indian, and Atlantic Oceans before impact. B: Deviations of water temperatures 231 d after impact with respect to preimpact values. C: Deviations 60 yr after impact. D: Deviations 2000 yr after impact.

temperature (Fig. 4), the oceans do not return to their previous state: 60 yr after impact, they are in an intermediate state. The SST deviations are still all negative except in one Atlantic cell at lat 50°N (Fig. 6C). We try to explain this behavior in the following section about the Atlantic circulation. Typical deviations with respect to preimpact temperatures are $\sim -0.1$ °C, but northern regions of the Atlantic show larger changes.

In the following 2000 yr, the state of the oceans converges to a new climatic equilibrium. After that time, the SSTs of the Southern Hemisphere are higher than before the impact, while the surface temperatures of the Atlantic and Pacific from lat 20°S to 45°S latitude are lower (Fig. 6D). However, in the new steady state the surfaces of Pacific and Atlantic north from lat 45°S are warmer than before the impact.

### *Sea temperature profiles*

The horizontal currents in the uppermost tens of meters of the oceans are affected by atmospheric winds at the surface, resulting in a typical water velocity of 1 m/s. In deeper layers, horizontal and vertical motions of the water are driven by density gradients, which depend on temperature and salinity. The water and heat exchanges induced by these currents occur on time scales much longer than the atmospheric time scales. While the residence time of water at the surface is some months, it amounts to ~100 yr for the uppermost 100 m, and the age of deep water is ~1000 yr (von Reden et al., 1997). Therefore, the vertical transport of temperature anomalies is slow compared with the lifetime of the bolide-induced dust cloud.

Figure 7A shows water temperatures as function of depth in the equilibrium state of the model before the impact. Months after the impact the temperature deviations are largest at the surface (Fig. 7B). They are −2.4 °C, −1.9 °C, and −1.7 °C for Indian, Atlantic, and Pacific, respectively, and reduce to ~−0.5 °C at a depth of 200 m. Below 400 m, the water temperatures have not changed: 60 yr after impact (Fig. 7C), temperature deviations appear down to 4 km depth, although the largest changes occur only in the uppermost 700 m. At the surface, all three basins are colder than before the impact. The cooling increases with depth in the Pacific down to 400 m. From there to the bottom, the deviations are still negative but small. In the Indian Ocean, they are negative and small at all depths. A zone in the Atlantic down to 800 m exhibits warmer temperatures with a peak value of +0.5 °C at 100 m. After 2000 yr (Fig. 7D) the temperatures have risen above those preceding the impact, except in the uppermost 200 m of the Pacific. It is interesting that the increase of temperature by 0.5 °C in the Atlantic 100 m below the surface remains.

### *Atlantic circulation and temperature*

Figure 8 shows the Atlantic stream function, the contours of which are parallel to the motion of the water. The flow is dominated by a basin-wide overturn circulation. In a layer from the surface to a depth of 500–1000 m, it transports warm water from southern and equatorial to northern regions, where the temperature differences of the warm water and the cold atmosphere induce high evaporation rates. Consequently, the ocean temperature drops and salinity increases. Both effects increase the density of the water, which in turn sinks to deep sea levels in the northern Atlantic. Below 1500 m depth the water flows southward and upwells again. South of the equator, a local second circulation rotates in the opposite direction. It transports water from the equator to lat 30°S, where the water is advected back to the equator at a depth of a few hundred meters. A symmetrical third local current in the Northern Hemisphere is superimposed over the large first basin-wide circulation. At the surface, the net effects of these three currents are (1) ascending water at the equator from several 100 m below, (2) subsiding water from 20°N to 40°N and 20°S to 40°S latitude in both hemispheres, (3) a fast horizontal transport of surface water from the equator to 20°N and 20°S latitude, and a slow horizontal surface motion in the northern Atlantic from 20°N to the poles. Due to the circulation, the impact-induced cooling in the surface water layers are advected vertically.

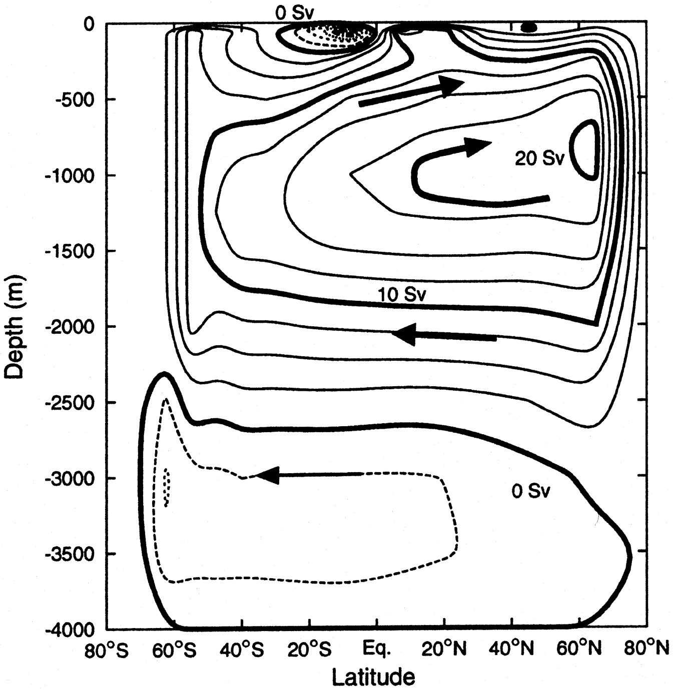

Figure 8. Latitude-depth section of stream function in Atlantic before impact. Unit is 1 Sv (Sverdrup) = $10^6$ m$^3$/s. Motion of water is parallel to isolines of stream function. Contour interval is 2.5 Sv. Amount of water flowing between two contours is equal to difference of values of stream function. Positive and negative values are represented by solid lines and dashed lines, respectively.

Figure 9 shows the steady-state temperatures in the Atlantic before the impact. Temperature deviations 231 d after the impact are given in Figure 10. At 20°S and 30°N latitude, the deviations have advanced further downward than at the equator, which is explained by the equatorial upwelling and the subsiding waters from 20°N to 40°N and 20°S to 40°S latitude. There are nearly no changes in subsurface temperatures in the polar regions, because there the surface temperature changes are much smaller than at the equator.

The Atlantic temperatures of the steady state 2000 yr later show an increase at 200 m below the surface at lat 40°N with maximum temperature deviation of more than +3 °C (Fig. 11). In the steady state before the impact, potential instabilities in the northern Atlantic generated mixing of water from vertically adjacent cells. This mixing process convected warm water from a depth of 100 m toward the surface. However, the instabilities between lat 20°N and 45°N have disappeared 2000 yr after the impact. Thus the vertical mixing and the related warm water transport to the surface stop in this region, which is a significant change in the thermohaline circulation. Therefore, we observe the strongly negative temperature deviation at the Atlantic surface at lat 40°N (Fig. 6D). However, the potential instabilities and the vertical mixing have not disappeared north from lat 45°N. Because of the increased temperature in the subsurface cell in the northern Atlantic (Fig. 11), the mixing transports warmer water to the surface. Hence, the mixing gives rise to the peak in the SST (Fig. 6D) at lat 50°N.

The basin-wide pattern of the circulation remains, although during the 2000 year transition the strength of the Atlantic overturn circulation (Fig. 8) shows an oscillation with a period of 200 yr. This oscillation is model related (Aeberhardt et al., 2000) and may not reflect a natural behavior of the ocean.

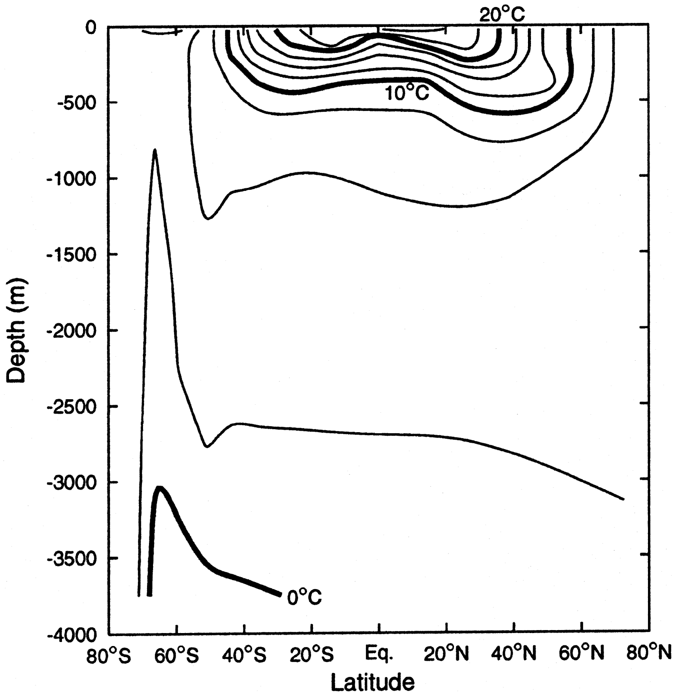

Figure 9. Temperature-latitude-depth section in Atlantic before impact. Contour interval is 2.5 °C.

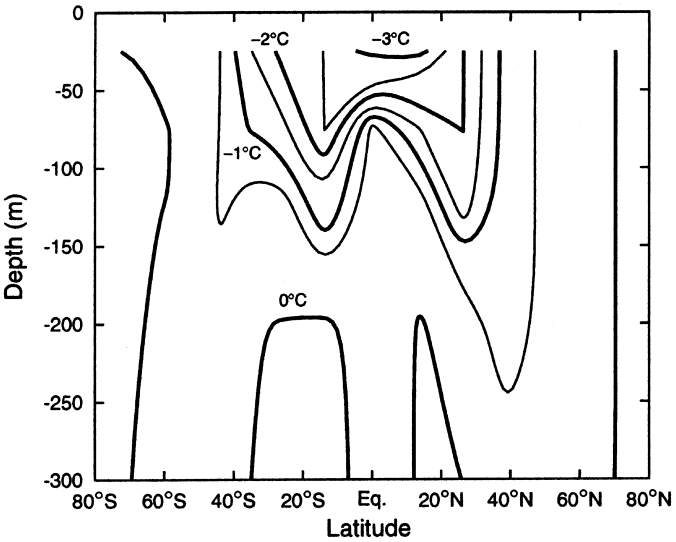

Figure 10. Deviations of temperature field in uppermost 300 m of Atlantic 231 d after impact with respect to values in equilibrium state before impact (Fig. 9). Largest cooling appears near equator at surface. Below 250 m deviations are smaller than 0.5 °C. Contour interval is 0.5 °C.

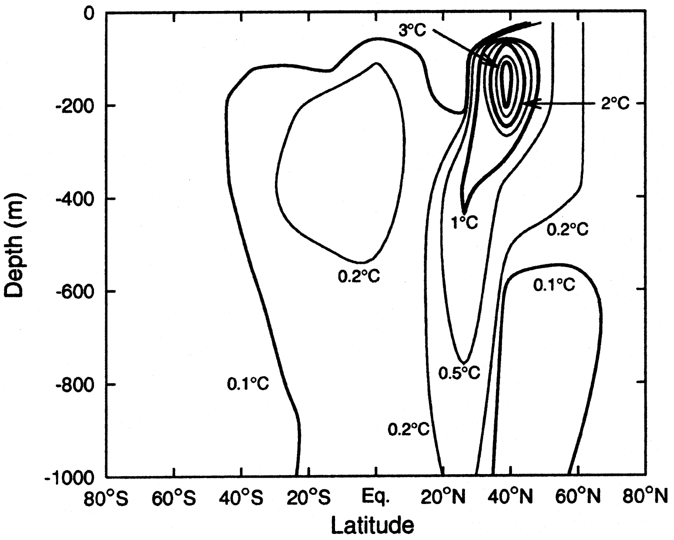

Figure 11. Deviations of temperature field in uppermost 1000 m of Atlantic 2000 yr after impact with respect to values before impact (Fig. 9). Except for cell with increased temperatures at 40° N latitude, differences are below 0.5 °C.

### *Air temperatures over the oceans*

Due to its smaller heat capacity, the temperature of the air over the ocean changes much more rapidly than the water temperature following a change in input energy. Figure 12 shows deviations of air temperatures in three latitudinal bands near the north pole, the equator, and the south pole. In the first 50 d, the polar air temperatures increase by 5 °C (north) and 6 °C (south). This response is probably caused by the radiative insulation provided by the dust, which is most effective for low solar positions or during nighttime (Fig. 3, B and C), and therefore in the polar regions. The equatorial air temperature is increased during ~2 months; however, the peak of more than 1 °C is reached 9 d after the impact. The following phase of colder equatorial temperature lasts for more than 5 months, before the minimum value is reached at a time corresponding to the lowest SSTs (Fig. 5). The lowest temperature is 3 °C below the preimpact value. These results compare with the climate simulations by Covey et al. (1994), who used a general atmospheric circulation model coupled to a thermodynamic model of the upper mixed layer of the oceans, to consider climatic effects of dust generated by an impact. Their simulation started with a dust load being 50 times larger than the one considered here, which corresponds to an impactor diameter of 17.5 km according to equation 1 and an assumed density of 3000 kg/m$^3$. They investigated large-particle and small-particle scenarios; the small-particle scenario compares with the dust particle sizes used in this study. For the temperatures of air over oceans at the end of 1 yr, coolings of 6 °C and 4 °C were found for the large-particle and small-particle scenario, respectively. In the polar regions, their simulation showed increased temperatures between 0 °C and more than 10 °C compared to their control case in the period from 10 to 20 days after impact. After 1 yr, positive and negative temperature deviations occur in Antarctica as well as in the arctic region.

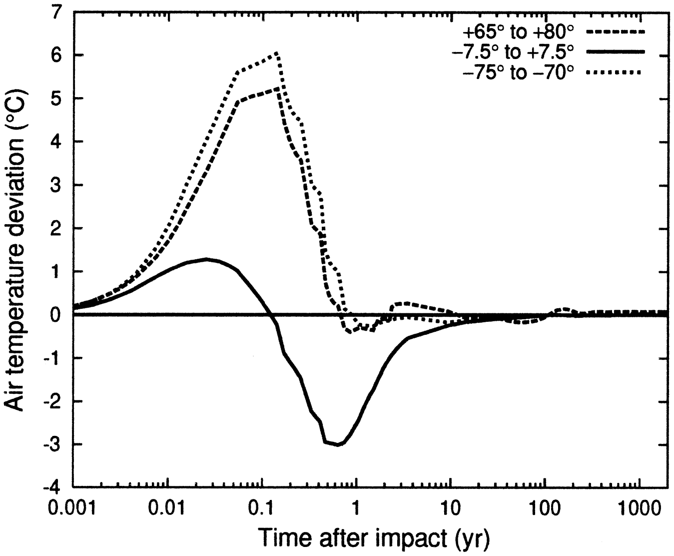

Figure 12. Deviations of air temperatures over sea in three latitudinal bands: (A) 75°S to 70°S, (B) 7.5°S to 7.5°N, and (C) 65°N to 80°N. Amplitude of cooling in equatorial region is ~3 °C. Air temperatures in polar latitudinal bands increase by 5 °C and 6 °C, respectively, within first 50 d and return to preimpact values in <1 yr. Temperatures before impact are −6.4 °C, 26.7 °C, and −4.5 °C for southern, equatorial, and northern regions, respectively.

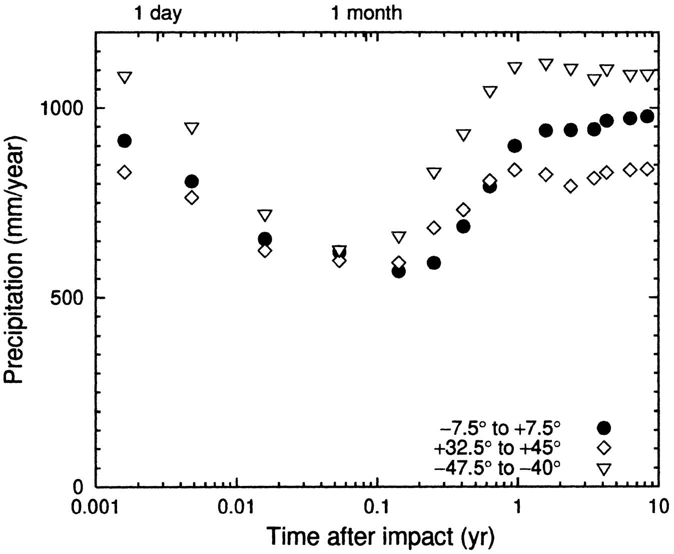

Figure 13. Precipitations after impact in three latitude bands.

### *Precipitation*

Covey et al. (1994) noted a collapse of the hydrological cycle in their simulations. They reported that the globally averaged precipitation decreases by 90% after 3 months and remains below 50% after 1 yr. We find a smaller decrease in precipitation. Figure 13 shows precipitation rates as function of time after the impact in three latitude bands located at the equator and in the Northern and Southern Hemispheres. The reduction of precipitation is <50%, and the minimum is reached in the first 2 months. After 1 yr, deviations of precipitation rates are within 10% of original value. The determination of evaporation and precipitation rates was given in Stocker et al. (1992).

## CONCLUSIONS

In this chapter we investigated impact-induced climate changes over 2000 yr by using a model that includes dust settling and coagulation, radiation transfer, and ocean-atmosphere coupling. The amount of dust injected into the atmosphere corresponds to an impactor with a diameter of 5 km, assuming a density of 3000 kg/m$^3$.

In the first year, equatorial SSTs dropped by −3 °C, while the polar SSTs showed much smaller deviations: 500 m below the surface of the oceans, temperatures remained unchanged. Air temperatures dropped (−3 °C) with the exception of the polar regions (+6 °C). Precipitation decreased in 3 months to 50%, but recovered within 1 yr.

The climate is a system with more than one equilibrium. Once it has been pushed out of one equilibrium state due to the large amount of dust in the atmosphere, it will settle over time into a new equilibrium that does not necessarily coincide with the initial one. The reasons are the large oceanic heat inertia and the complexity of the system. Therefore, the climatic response operates on time scales different from the short-term radiative forcing due to dust studied here. The time scales of some of the climatic excursions, which are initiated by the perturbed atmospheric energy fluxes, range from fractions of 1 yr to hundreds of years. For example, 2 yr after impact, deviations of air and SSTs were still ~−1 °C, and after 60 yr the amplitudes were reduced to 0.1 °C. On long time scales, the ocean circulation advected the temperature anomalies from the surface to the depth. Because such transport is slow, there is a considerable time lag between the surface changes and response of deeper zones. The major deviations were still restricted to depths above 1000 m 60 yr after the impact. On average, the deep-sea temperatures started changing only after ~100 yr. The climate took more than 2000 yr to reach a new steady state.

Both ocean circulation and temperatures changed as part of the global climate changes. During the first millennium after the impact the strength of the Atlantic overturning circulation showed a damped oscillation. Therefore the transport of surface waters toward the bottom was not constant, which may disturb global cycles such as the carbon and the oxygen cycles. After 2000 yr, the main new feature in the circulation pattern was a weaker convection zone in the northern Atlantic.

An extreme climatic scenario is the glaciation of vast areas. However, we did not observe growth or formation of sea ice shields. At the poles the cooling was too small, and in the middle and low latitudes the ocean temperatures did not drop below freezing.

## ACKNOWLEDGMENTS

We thank Karen Bice and David Kring for their helpful reviews. This work has been supported in part by the Swiss National Science Foundation.

## REFERENCES CITED

Aeberhardt, M., Blatter, M., and Stocker, T.F., 2000, Variability on the century time scale and regime changes in a stochastic forced zonally averaged ocean-atmosphere model: Geophysical Research Letters, v. 27, p. 1303–1306.

Argyle, E., 1988, The global fallout signature of the K/T bolide impact: Icarus, v. 77, p. 220–222.

Berk, A., Bernstein, L.S., and Robertson, D.C., 1989, MODTRAN: A Moderate Resolution Model for LOWTRAN 7: Hanscom Air Force Base, Massachusetts, Air Force Geophysics Laboratory Technical Report GL-TR-89–0122, 11 p.

Chokshi, A., Tielens, A.G.G.M., and Hollenbach, D., 1993, Dust coagulation: Astrophysical Journal, v. 407, p. 806–819.

Covey, C., Ghan, S.J., and Walton, J.J., 1990, Global environmental effects of impact-generated aerosols: Results from a general circulation model, *in* Sharpton, V., and Ward, P., eds., Global catastrophes in Earth history: Geological Society of America Special Paper 247, p. 263–270.

Covey, C., Thompson, S.L., Weissman, P.R., and MacCracken, M.C., 1994, Global climatic effects of atmospheric dust from an asteroid or comet impact on Earth: Global and Planetary Change, v. 9, p. 263–273.

Dominik, C., and Tielens, A.G.G.M., 1997, The physics of dust coagulation and the structure of dust aggregates in space: Astrophysical Journal, v. 480, p. 647–673.

Durda, D.D., Kring, D.A., Pierazzo, E., and Melosh, H.J., 1997, Model calculations of the proximal and globally distributed distal ejecta from the Chicxulub impact crater [abs.]: Lunar and Planetary Science Conference, 28th, Houston, Texas, Lunar and Planetary Institute, p. 315–316.

Farlow, N.H., Oberbeck, V.R., Snetsinger, K.G., Ferrey, G.V., Polkowski, G., and Hayes, D.M., 1981, Size distribution and mineralogy of ash particles in the stratosphere from eruptions of Mount St. Helens: Science, v. 211, p. 832–834.

Goody, R.M., and Yung, Y.L., 1989, Atmospheric radiation, theoretical basis (second edition): New York, Oxford University Press, 519 p.

Hansen, J.E., and Travis, L.D., 1974, Light scattering in planetary atmospheres: Space Science Reviews, v. 16, p. 527–610.

Hills, J.G., Nemchinov, I.V., Popov, S.P., and Teterev, A.V., 1994, Tsunami generated by small asteroid impacts, *in* Gehrels, T., ed., Hazards due to comets and asteroids: Tucson, University of Arizona Press, p. 779–789.

Hoffman, P.F., Kaufman, A.J., Halverson, G.P., and Schrag, D.P., 1998, A Neoproterozoic snowball Earth: Science, v. 281, p. 1342–1346.

Jaenike, R., 1988, Properties of atmospheric aerosols, *in* Fischer, G., ed., Landolt-Boernstein, New Series: Numerical data and functional relationships in science and technology, Group 5: Geophysics and space research, Volume 4: Meteorology, Sub-Volume B: Physical and chemical properties of the air: Berlin, Springer-Verlag, p. 405–428.

Kneizys, F.X., Shettle, E.P., Abreu, L.W., Chetwynd, J.H., Anderson, G.P., Gallery, W.O., Selby, J.E.A., and Clough, S.A., 1988, Users Guide to LOWTRAN 7: Hanscom Air Force Base, Massachusetts, Air Force Geophysics Laboratory, AFGL-TR-88-0177, 137 p.

Kring, A.H., Melosh, H.J., and Hunten, D.M., 1996, Impact-induced perturbations of atmospheric sulfur: Earth and Planetary Science Letters, v. 140, p. 201–212.

Lewis, J.S., Watkins, G.H., Hartmann, H., and Prinn, R.G., 1982, Chemical consequences of major impact events on Earth, *in* Silver, L.T., and Schultz, P.H., eds., Geological implications of impacts of large asteroids and comets on the Earth: Geological Society of America Special Paper 190, p. 215–221.

Liou, K.N., 1980, An introduction to atmospheric radiation: New York, Academic Press, 392 p.

Melosh, H.J., Schneider, N.M., Zahnle, K.J., and Latham, D., 1990, Ignition of global wildfires at the Cretaceous/Tertiary boundary: Nature, v. 343, p. 251–254.

Morrison, D., Chapman, C.R., and Slovic, P., 1994, The impact hazard, *in* Gehrels, T., ed., Hazards due to comets and asteroids: Tucson, University of Arizona Press, p. 59–91.

Otto, E., Fissan, H., Park, S.H., and Lee, K.W., 1999, The log-normal size distribution theory of brownian aerosol coagulation for the entire particle size range. 2. Analytical solution using Dahneke's coagulation kernel: Journal of Aerosol Science, v. 30, p. 17–34.

Pierazzo, E., Kring, D.A., and Melosh, H.J., 1998, Hydrocode simulation of the Chicxulub impact event and the production of climatically active gases: Journal of Geophysical Research, v. 103, p. 28 607–28 625.

Pope, K.O., Baines, K.H., Ocampo, A.C., and Ivanov, B.A., 1994, Impact winter and the Cretaceous/Tertiary extinctions: Results of a Chicxulub asteroid impact model: Earth and Planetary Science Letters, v. 128, p. 719–725.

Pope, K.O., Baines, K.H., Ocampo, A.C., and Ivanov, B.A., 1997, Energy, volatile production, and climatic effects of the Chicxulub Cretaceous/Tertiary impact: Journal of Geophysical Research, v. 102, p. 21 645–21 664.

Prinn, R.G., and Fegley, B., Jr., 1987, Bolide impacts, acid rain, and biospheric traumas at the Cretaceous-Tertiary boundary: Earth and Planetary Science Letters, v. 83, p. 1–15.

Ramaswamy, V., and Kiehl, J.T., 1985, Sensitivities of the radiative forcing due to large loadings of smoke and dust aerosols: Journal of Geophysical Research, v. 90, p. 5597–5613.

von Reden, K.F., McNichol, A.P., Peden, J.C., Elder, K.L., Gagnon, A.R., and Schneider, R.J., 1997, AMS measurements of the $^{14}$C distribution in the Pacific Ocean: Nuclear Instruments and Methods in Physics Research B, v. 123, p. 438–442.

Stocker, T.F., Wright, D.G., and Mysak, L.A., 1992, A zonally averaged, coupled ocean-atmosphere model for paleoclimate studies: Journal of Climate, v. 5, p. 773–797.

Toon, O.B., Pollack, J.B., Ackermann, T.P., Turco, R.P., McKay, C.P., and Liu, M.S., 1982, Evolution of an impact-generated dust cloud and its effects on the atmosphere, *in* Silver, L.T., and Schultz, P.H., eds., Geological implications of impacts of large asteroids and comets on the Earth: Geological Society of America Special Paper 190, p. 187–200.

Toon, O.B., Zahnle, K.J., Morrison, D., Turco, R.P., and Covey, C., 1997, Environmental perturbations caused by the impacts of asteroids and comets: Reviews of Geophysics, v. 35, p. 41–78.

Ward, S.N., and Asphaug, E., 2000, Asteroid impact tsunami: A probabilistic hazard management: Icarus, v. 145, p. 64–78.

Williams, D.M., Kasting, J.F., and Frakes, L.A., 1998, Low-latitude glaciation and rapid changes in the earth's obliquity explained by obliquity-oblateness feedback: Nature, v. 396, p. 453–455.

Wolbach, W.S., Gilmour, I., and Anders, E., 1990, Major wildfires at the Cretaceous/Tertiary boundary, *in* Sharpton, V., and Ward, P., eds., Global catastrophes in Earth history: Geological Society of America Special Paper 247, p. 391–400.

Wright, D.G., and Stocker, T.F., 1992, Sensitivities of a zonally averaged global ocean circulation model: Journal of Geophysical Research, v. 97, p. 12 707–12 730.

Wurm, G., and Blum, J., 1998, Experiments on preplanetary dust aggregation: Icarus, v. 132, p. 125–136.

Zahnle, K.J., 1990 Atmospheric chemistry by large impacts, *in* Sharpton, V., and Ward, P., eds., Global catastrophes in Earth history: Geological Society of America Special Paper 247, p. 271–288.

MANUSCRIPT SUBMITTED OCTOBER 10, 2000; ACCEPTED BY THE SOCIETY MARCH 22, 2001

Printed in the U.S.A.